

Noninvasive In Vivo MRI Detection of Neuritic Plaques Associated with Iron in APP[V717I] Transgenic Mice, a Model for Alzheimer's Disease

G. Vanhoutte,^{1*} I. Dewachter,² P. Borghgraef,² F. Van Leuven,² and A. Van der Linden¹

Transgenic mice overexpressing the London mutant of human amyloid precursor protein (APP[V717I]) in neurons develop amyloid plaques in the brain, thus demonstrating the most prominent neuropathological hallmark of Alzheimer's disease. In vivo 3D T_2^* -weighted MRI on these mice (24 months of age) revealed hypointense brain inclusions that affected the thalamus almost exclusively. Upon correlating these MRI observations with a panel of different histologic staining techniques, it appeared that only plaques that were positive for both thioflavin-S and iron were visible on the MR images. Numerous thioflavin-S-positive plaques in the cortex that did not display iron staining remained invisible to MRI. The in vivo detection of amyloid plaques in this mouse model, using the intrinsic MRI contrast arising from the iron associated with the plaques, creates an unexpected opportunity for the noninvasive investigation of the longitudinal development of the plaques in the same animal. Thus, this work provides further research opportunities for analyzing younger APP[V717I] mouse models with the knowledge of the final outcome at 24 months of age. Magn Reson Med 53:607–613, 2005. © 2005 Wiley-Liss, Inc.

Key words: Alzheimer's disease; amyloid plaques; mouse; iron; in vivo MRI

Alzheimer's disease (AD) is characterized by a progressive decline of cognitive function, while the neuropathologic features include the occurrence of neurofibrillary tangles, neuritic plaques, decreased synaptic density, and loss of neurons. Neuritic plaques consist of extracellular β -amyloid (A β) deposits surrounded by dystrophic neuritis (1). The plaques are neurotoxic and induce inflammatory responses. According to the amyloid cascade hypothesis, the increased amyloid deposition results in the onset and progression of AD (2,3,4,5) and therefore amyloid plaques became crucial as a target for many therapeutic approaches (6,7).

Despite the impact of in vivo imaging techniques in daily clinical practice and also in neuroscience, typical Alzheimer plaques were never visualized in vivo in patients. To diagnose AD and to differentiate from other dementias, the detection of at least one typical hallmark, i.e., amyloid plaques or neurofibrillary tangles, appears

essential. To date, accumulations of amyloid in AD patients have been observed only postmortem. Recently, however, significant progress has been made visualizing AD plaques using transgenic mouse models for AD. Skovronsky et al. (8) reported in vivo labeling of amyloid plaques in transgenic mice using a radiolabeled ligand but detection was still performed postmortem with fluorescence microscopy. Another attempt to demonstrate plaques postmortem used MRI and was based on injection of a specific derivative of the amyloid peptide with a high molecular specificity for amyloid as a label, i.e., putrescine-gadolinium-A β (9). Finally, Wadghiri et al. (10) used systemic injection of monocrystalline iron oxide nanoparticles or gadolinium (Gd) labeled A β 1–40 peptide with a high affinity for A β and were able to detect ex vivo but also in vivo amyloid plaques in the affected mouse brains. In this approach, the main obstacle for amyloid labeling remains the blood brain barrier and its transient opening using mannitol must be considered quite invasive. Another drawback may be the authentication of amyloid plaques and the exclusion of the involvement of blood vessels embedded with contrast agent, which requires subsequent histology of the brain.

The first MRI study that demonstrated amyloid plaques without any exogenous labeling was performed by Benveniste et al. in 1999 (11). Three dimensional T_2^* images of postmortem human AD brain samples, acquired in more than 2.7 hr, revealed dark spots in the brain correlating with histologic amyloid staining. Recently, using T_2 MR contrast, identification of plaque-like structures in the cortex and hippocampus of fixed mouse brain was reported by Zhang et al. (12). However, the authors did not explain the source of the MR contrast in relation to the physiologic processes related with plaque formation and the evidence was only confirmed by the subsequent co registration of plaques by histology. Analogous to this finding, Helpert et al. (13) demonstrated a reduced T_2 value in the cortex and hippocampus in vivo in an AD mouse model, but individual distinguishable plaques could only be discerned on in vitro high-resolution T_2 -weighted images of the fixed mouse brain.

This paper introduces the first in vivo observation of plaques in an AD mouse model without any use of external labeling. The observations are exclusively based on T_2^* contrast, which makes this a noninvasive approach. It confirms the observations of others (12) but goes beyond these observations by revealing that iron is the source of this T_2^* contrast. The study is performed on the APP[V717I] transgenic mice model and extends it into a suitable model for MRI studies, which focus on amyloid plaques, either for therapeutic follow up studies or to

¹Bio-Imaging Lab, UA, Antwerp, Belgium.

²Experimental Genetics Group, KULeuven, Leuven, Belgium.

Grant sponsor: special research fund (BOF-NOI) of the University of Antwerp; Grant sponsor: Fund for Scientific Research-Flanders; Grant sponsor: Rosa Blankaert Fund of the University of Antwerp; Grant sponsor: Research Fund of the University of Leuven, KUL.

*Correspondence to: Greetje Vanhoutte, Groenenborgerlaan 171, Bio-Imaging Lab, 2020 Antwerpen, Belgium.
E-mail: Greetje.Vanhoutte@ua.ac.be

Received 18 June 2004; revised 8 October 2004; accepted 9 October 2004.

DOI 10.1002/mrm.20385

Published online in Wiley InterScience (www.interscience.wiley.com).

© 2005 Wiley-Liss, Inc.

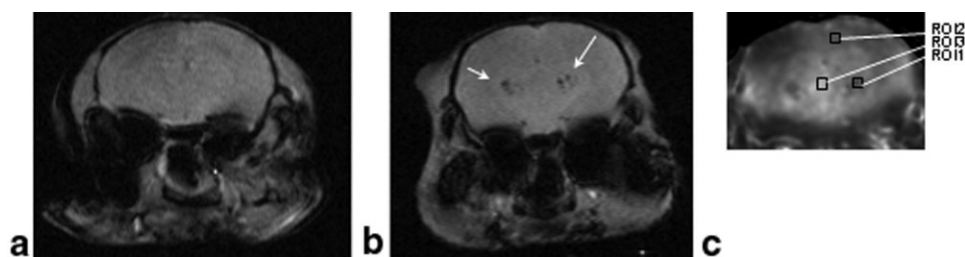


FIG. 1. In vivo 2D GE MRI (TR/TE:500 ms/8 ms) for comparison between (a) WT and (b) APP[V717I] Tg mice. Hypointense anomalies appeared exclusively in the thalamus region of Tg mice (white arrows). A representative T_2^* map of an APP[V717I] mouse model generated from in vivo MRI data acquired with TE 5, 8, and 15 ms is illustrated in (c). In APP[V717I] brain, the ventral thalamic nuclei (ROI1) have a T_2^* value of 35.23 ± 2.96 ms, which is significantly lower compared to the T_2^* value of 71.38 ± 1.48 ms for the same ROI in WT. No difference in T_2^* was observed between WT and APP[V717I] brain when comparing the cingulate cortex (ROI2) (61.48 ± 2.64 ms versus 60.45 ± 3.56 ms) and central thalamic nuclei (ROI3) (75.84 ± 2.17 ms versus 82.64 ± 2.97 ms)

obtain information on the propensity of amyloid to accumulate iron. Defective iron homeostasis, resulting in increased iron levels in the brain, has been reported as common in AD and other neurodegenerative disorders (14,15). In AD brain, iron appeared to become particularly concentrated in amyloid plaques and it was suspected to catalyze formation of free radicals (16). Iron-loaded amyloid plaques, detectable by in vivo MRI, could therefore become a useful indication for AD.

MATERIALS AND METHODS

Animal Model

Transgenic mice overexpressing the London mutant of human amyloid precursor protein APP[V717I] in neurons suffer from early (3 months) cognitive deficits, while reproducing robustly and faithfully the amyloid pathology in the brain of AD patients (17). This experimental model for AD develops diffuse and senile amyloid plaques in the brain parenchyma from 12 months onward, followed at 15–18 months by the equally typical cerebrovascular amyloid angiopathy (18,19). At 2 years of age the brains of surviving APP[V717I] transgenic mice all have hallmarks of the amyloid pathology, similar to the brains of AD patients.

MRI Experiment

MRI was performed on these APP[V717I] transgenic mice using a MR microscope (MRRS, Guildford, UK) with a 7-T horizontal-bore magnet and 8-cm aperture self-shielded gradients with a strength of 0.1 T/m (Oxford Instruments). A customized headphone RF transmission antenna and a circular surface receive antenna (ϕ : 20 mm) was positioned in a reproducible manner on the head of the mice. This was fixed in an animal restrainer with ear bars and a tooth bar. Four APP[V717I] Tg mice and 4 wild-type (WT) age-matched (24 months) controls were anesthetized using 0.4% isoflurane in a mixture of O_2 : N_2O (3:7) at a flow rate of 600 mL/min. Body temperature was monitored and maintained between at $37.0 \pm 0.2^\circ\text{C}$ using a rectal temperature probe with feed back to an electrical heating circuit. Mice were not ventilated but end-tidal CO_2 (3.5%) and breaths per minute (180) were registered with a microcapnometer (Linton Instruments, UK).

Three dimensional T_2^* -weighted GE images, covering a brain volume of $(20 \times 20 \times 15)$ mm³, were acquired within 68 min (TR 500 ms, $256 \times 128 \times 64$). This allowed a short anesthesia period after which all mice recovered completely. The corresponding digital voxel resolution is $(78 \times 156 \times 234)$ μm^3 . The MR data set was reconstructed to an image matrix of $(256 \times 256 \times 256)$, resulting in 256 coronal slices of 58 μm thickness. Pixel dimensions in plane were (78×156) μm^2 as acquired and (78×78) μm^2 as displayed. Next to 3D imaging, which provides anatomic information, we also took images with increasing T_2^* -weighting (TE = 5 ms, 8 ms, 15 ms) to calculate T_2^* maps. Following in vivo MRI measurements, brains were dissected and immersion-fixed overnight in 4% paraformaldehyde phosphate-buffered saline (PBS) to perform in vitro 3D GE MRI of the entire fixed brain with a longer acquisition time ($256 \times 256 \times 128$), thus resulting in a higher power of resolution and signal-to-noise ratio.

Histology:

Coronal vibratome sections (40 μm) were cut and processed to perform thioflavin-S staining according to standard protocols (20). Prior to the thioflavin-S staining, slices were stained with 2% potassium ferrocyanide for iron detection.

RESULTS

In vivo 2D GE MRI revealed a remarkable difference between the brain of age-matched (24 months) WT mice and APP[V717I] Tg mice. The brains of APP[V717I] Tg mice displayed hypointense, globular anomalies distributed bilaterally in the thalamus (Fig. 1a and b) and occasionally in the subiculum. Quantifying the T_2^* values showed a significant reduction of the T_2^* values where these anomalies were localized. A T_2^* map from a typical APP[V717I] brain slice is shown in Fig. 1c. There exists a T_2^* heterogeneity across the slice with smoothly increasing values in the ventral direction. This heterogeneity is due to discontinuities in the magnetic susceptibility from different materials, which gives rise to macroscopic magnetic field gradients that cannot be eliminated by shimming. T_2^* is magnetic field strength dependent and may also depend on difference in species.

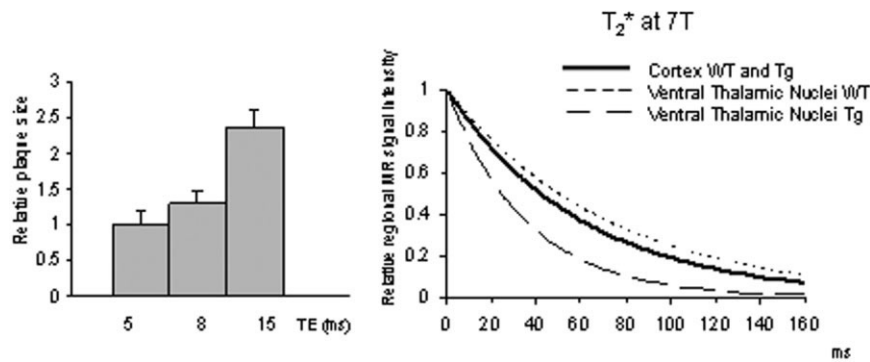


FIG. 2. (Left) Relative change in plaque size as measured in in vivo T_2^* -weighted images of APP[V717I] mouse brain ($n = 4$). A clear increase in size of the hypointense plaque-like structure (up to 130%) was discerned with increasing TE of 10 ms. The T_2^* decay monoexponential curve ($M_{xy}(t) = M_{xy}(0) \exp(-t/T_2^*)$) for the cortex and the ventral thalamic nuclei is shown on the right. Compared with the WT mice, the APP[V717I] mice display a similar T_2^* decay in the cortex while the decay in the ventral thalamic nuclei is much faster.

T_2^* values were calculated in three different brain regions (cortex, ventral thalamic nuclei, and central thalamic nuclei) selected on the T_2^* maps of WT and APP[V717I] mice. A reduction in T_2^* values of up to 50% was observed in the ventral thalamic nuclei, which contained the hypointense anomalies. More evidence illustrating that T_2^* is affected is found by estimating the size of the anomalies at different TE while delineating its boundaries using thresholding. Series of MR images with increasing TE (from 5 to 15 ms) showed an increasing size of the hypointense brain inclusions, i.e., a relative increase up to 130% (Fig. 2). The TE-dependent signal decay can be modeled with a monoexponential function as illustrated in the graph in Fig. 2. This graph shows the similarity of cortex T_2^* decay in both WT and APP[V717I] models. Thus, our T_2^* approach appears quite accurate with the more rapid T_2^* decay in the ventral thalamic nuclei of the APP[V717I] models significantly different from WT.

The anomalies were clearly visible on both the in vivo and in vitro 3D images of the brain of all APP[V717I] transgenic mice. The in vitro images displayed better defined boundaries and smaller anomalies due to the higher in-plane digital spatial resolution. Figure 3 shows an accurate match between in vitro MRI (Fig. 3a) and the cor-

responding histologic sections stained with thioflavin-S (Fig. 3b). Images were coregistered visually by using carefully delineated anatomically distinctive structures such as the lateral ventricle (LV), the hippocampal fissure (hif), and even smaller white fiber tracts such as the mammillothalamic tract (mt), which was discernable on both MRI and histologic sections. The comparison revealed an identical distribution pattern of thioflavin-S-positive amyloid plaques in the thalamus, confirming that the observed hypointense anomalies were neuritic amyloid plaques.

Histologic analyses, using two different staining techniques, demonstrated additional smaller amyloid plaques in the cortex and hippocampus, which did not generate anomalies detectable by MRI. Staining of adjacent serial brain sections for iron, as performed earlier on the brain of AD patients (18,20), demonstrated that the majority of the plaques in the thalamus were positive for iron (Fig. 3c, d, e, and f).

Since the coronal vibratome sections have a smaller slice thickness (40 μm) than the MR zero-filled image slices (58 μm), accurate matching of the two image modalities is assisted by detailed anatomic reference points. Moreover, since the MR visibility of the amyloid plaques seems to rely on its iron content providing susceptibility contrast, the MRI probably provides an overestimation of

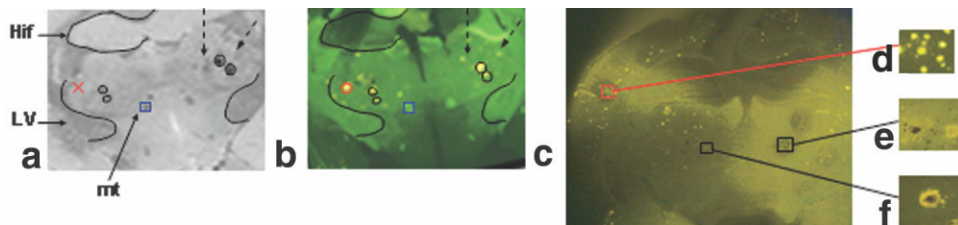


FIG. 3. (a) In vitro MR image (in-plane resolution of 58 μm) revealing anatomic details such as mammillothalamic tract (mt, box), hippocampal fissure (hif), and the lateral ventricle (LV), which were used as reference points for comparison with histologic thioflavin-S-stained section (b). The black circles illustrate perfect correlation based on cursor analyses between hypointense spherical inclusions on the MR images and the stained plaques on the corresponding histologic section. More tiny stained plaques on the histologic slice (dashed arrows) correspond to a spotted inhomogeneous area on the corresponding MRI. Also, one large plaque, stained on the histologic slice, is missing on the corresponding MRI (red cross). In (c) a representative iron-stained histologic brain slice of an APP[V717I] mouse shows details from the cortex (d) and the ventral thalamic nuclei (e, f). The staining of iron is observed as a dark core in the bright stained plaques and exclusively present in the thalamic amyloid plaques.

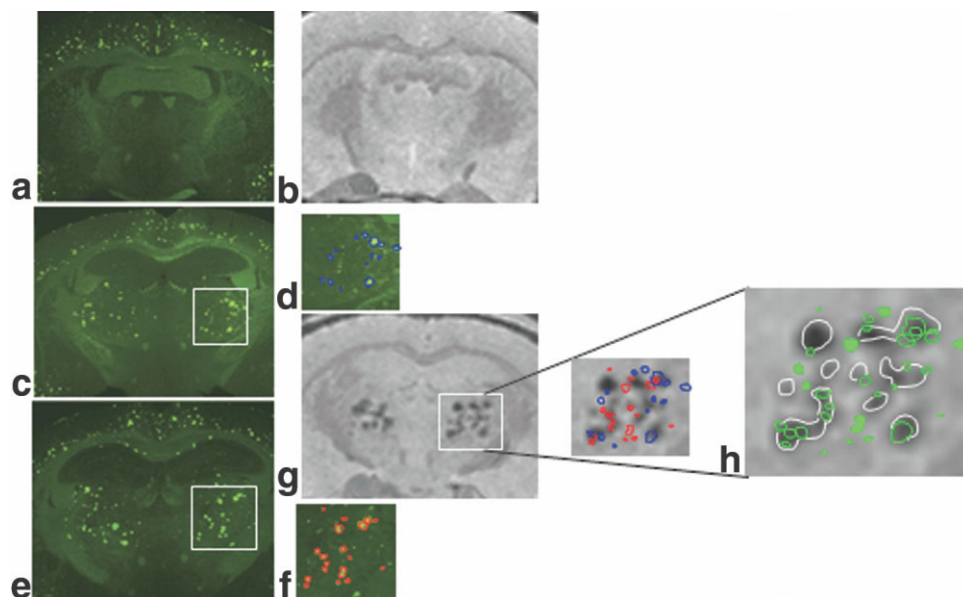


FIG. 4. A histologic brain slice of an APP[V717I] mouse, obtained at -0.8 mm from the bregma, showing numerous thioflavin-S-stained plaques in the cortex (a) while the correlating MR GE image displays no abnormal contrast (b). Two adjacent thioflavin-S-stained brain sections obtained -2 mm from the bregma (c and e) illustrate the occurrence of amyloid plaques in the cortex and the thalamic areas. The corresponding MR GE image displays numerous hypointense brain inclusions exclusively in the thalamus region (g). Overlaying the individually stained plaques of two ROIs (boxes d and f) delineated in blue and red, respectively, results in a two-colored compilation (h), allowing more accurate correlation of the thioflavin-S-positive spots with the corresponding MRI abnormalities. The hypointense anomalies (delineated in white) and the associated thioflavin-S-stained plaques (delineated in green) show that several smaller sized clustered plaques result in one larger hypointense area on the MRI. Bold green spots do not have a correlate on the MRI and probably do not contain Fe. The top left section in h represents a quite large MRI anomaly (white) compared to the tiny histologic plaque size (green). It is assumed that the next histologic slice will reveal a more robust plaque whose susceptibility influence expands to this MRI slice. The same holds for the other MRI anomalies, which remained without a histologic correlation.

the real plaque size. To obtain a more accurate correlation, we combined the information of two adjacent histologic sections and matched it with the hypointense brain inclusions on the MRI. Figure 4a and b represent, respectively, the histologic slice and the corresponding MR image in coronal position, obtained at the coordinate -0.8 mm from the bregma. At this position numerous tiny thioflavin-S-positive plaques, overwhelmingly present in the cortex, remain invisible on the MR GE image due to the absence of iron accumulation within these amyloid plaques as illustrated in Fig. 3d. The next two histologic sections in Fig. 4c and 4e display plaques in both the cortex and the thalamus region. The MR image at this position (bregma -2 mm) (Fig. 4g) reveals only anomalies in the thalamic region. At first sight, the hypointense inclusions mimic the histologic section with poor specificity. However, if we combine all the histologically stained plaques of the thalamus of two adjacent histologic slices (Fig. 4d and f) and overlay it on the MR image, the similarity between the two patterns becomes more obvious. The resulting image in Fig. 4h illustrates how the distribution of MR identified plaques is associated with the location of histologic stained plaques covering two slices. As expected from the susceptibility effects, the drawn (white) boundaries of the hypointense structures on the MRI often harbor numerous distinctive small histologic plaques. Histologic plaques associated with an MR identified plaque are shown with boundaries drawn in green (Fig. 4h). Green spots represent the small number of histologic identified plaques that do not overlay

exactly with hypointense abnormalities on the corresponding MRI slice. This could be due to their small size (diameter smaller than $78 \mu\text{m}$) or the absence of accumulated iron.

DISCUSSION

MRI Findings

The apparent absence of intrinsic MRI contrast changes characterizing the presence of amyloid plaques has thus far presented a serious limitation to the usefulness of MRI in the diagnosis and evaluation of Alzheimer's disease. Nevertheless, in 1999, Benveniste et al. (11,18) succeeded in showing evidence of plaques in very high-resolution T_2^* -weighted MRI scans of small fractions of brains of excised postmortem AD brain samples. Five years later identification of individual plaques relying on intrinsic MR parameters was still limited exclusively to in vitro observations of T_2 changes, which were then extended to various AD mouse models (10,12,13,18). Several efforts in developing MRI contrast agents designed to reveal AD plaques were, however, successful (9,10,13,18,21) but often associated with in vitro detection.

The present paper shows for the first time that plaques can be imaged in vivo, noninvasively using basic T_2^* -weighted MRI without the use of external contrast agents in a transgenic mice, which faithfully mimics the amyloid pathology of AD (APP[V717I]). By correlating our MRI

observations with a panel of different histologic staining techniques we have provided insight into the underlying cause of T_2^* reduction in the AD plaques in this mouse model. It appears that only plaques that were positive for both thioflavin-S and iron were visible on the MR images. Numerous thioflavin-S-positive plaques in the cortex that did not display iron staining remained invisible to MRI.

Using T_2^* as an intrinsic contrast parameter of the amyloid plaques, which is more rapid at high static magnetic field (7 T), the receiver bandwidth is increased and subsequently the signal-to-noise ratio decreases. This, together with the small voxel size in the 3D image modality, could give rise to visible susceptibility artifacts. However, the most enlightening thing about 3D imaging is the reduction of partial volume effects, i.e., preventing that different signal intensities coming from neighboring pixels merge. That is why, in our approach, all susceptibility-induced changes suspected to be amyloid plaques correlated with the iron staining.

Iron and Amyloid

Since a link between amyloid deposits and iron accumulation has been described (9,13,22), visualization of iron-loaded amyloid deposits in the brain (23,24,25,26,27) definitely provides a potential basis for the in vivo detection of amyloid deposits using intrinsic MRI contrast parameters. It must be stressed that although the number of plaques will be underestimated our data showed that the method never yielded false-positive results. Careful interpretation of MR data is still required since a possible second source of iron could be from red blood cells, but we did not observe any direct signs of cerebrovascular hemorrhages in the direct vicinity of the iron-loaded amyloid deposits nor anywhere else in the brain. This confirms our previous observations that despite extensive amyloid angiopathy, cerebrovascular bleeding is not a problem in this particular AD model (19).

The mechanisms that explain codeposition of amyloid and iron have been extensively investigated (28,29). Normal distributions of iron deposits in human and mouse lemur brain (30,31) have already been determined using T_2 -weighted MRI and signal intensity decrease correlated with Perl's staining for iron. The iron detection threshold at 1.5 T was established by Aoki et al. (32) and quantified as 10–15 mg/100 g. This does not, however, allow us to quantitatively determine the iron level with T_2 or T_2^* -weighted MRI since other factors also affect these parameters. It is known that the sensitivity of MRI to iron increases with magnetic field strength, since the T_2 signal is linearly dependent on the magnetic field strength (33). However, this relationship has never been investigated at strengths higher than 3 T (34) and, therefore, we cannot quantify the amount of iron in the thalamus. This makes T_2^* mapping an attractive approach for localizing small T_2^* changes that can help identify suspected regions of iron accumulation as they might be associated with plaque formation in AD pathology. Observations of analogous hypointense spots by in vivo and in vitro measurements refute the conclusion that senile plaques do not induce susceptibility effects in T_2^* -weighted MR images, as stated in a recent report that claimed the hypointense spots on MRI to be blood vessels (35). This author suggests that it

may be quite unusual, or even idiopathic, that the majority of amyloid plaques show susceptibility effects. In this case MRI would have very little impact on clinical evaluation of AD due to low sensitivity. In Fig. 4 we demonstrated that the MR contrast is based on susceptibility effects grouping distinctive histologic plaques covering 80 μm (two histologic slices) into MR hypointense inclusions in a 58- μm slice. There still remains a minority of histologic plaques that do not correlate with MR abnormalities. This is because of the combination of small size and the absence of iron accumulation. This is also true for the cortex plaques, which are invisible on MR GE images.

The extent to which our technique might be useful in humans with AD depends on the extent to which iron deposition occurs together with amyloid accumulation. Nevertheless, this approach is definitely applicable to the APP[717I] mouse model and provides an insight into previous reports on amyloid imaging, which could not explain the source of the observed T_2 MR contrast.

Thalamus versus Cortex

Our most peculiar observation, however, remains the exclusive labeling of amyloid deposits in the thalamus and its absolute absence in the cortex. It is possible that the structure of these plaques is different or that the microglia surrounding them are responsible for this phenomenon. According to Morris et al. (36,37), senile plaque staining for non-heme iron appears to be associated with glial cells. This makes the association of non-heme iron with the pathologic stigmata of AD a secondary response of glial cells, in particular microglia, to neuronal damage. This study of the APP[V717I] mouse model shows a discrepancy between cortex and thalamus plaques in iron loading. This might suggest that plaques in the cortex are at a different stage than those in the thalamus where glia cells are present due to ongoing inflammation processes. This could mean that the ability to image the effect of iron associated with amyloid plaques is plaque specific and gives additional information on the dynamics of the plaque formation and growth. Longitudinal studies of iron accumulation could therefore be very helpful in discerning differences in plaque stages.

Size Limits for Plaque Detection

The majority of the thioflavin-S-positive amyloid deposits have diameters ranging from 5 to 200 μm in the brain of transgenic AD mouse models. Therefore, to adequately resolve them, the spatial resolution of MRI has to be at least 200 μm , which is not a problem as we were able to take images with an in plane resolution of (78 \times 156) μm^2 . However, the iron gives these amyloid deposits a real bonus since it increases the susceptibility contrast, which extends beyond the size of the plaques. Our results even demonstrate that the imaging parameters (TE) can be manipulated to obtain an overestimation of the plaque size, which might become helpful to discern smaller plaques in this mouse model. This was underlined by the virtual increase in plaque size on the MRI images with increasing echo time (from 5 to 15 ms).

T_2^* contrast can originate from different sources and this might provide false-positive AD diagnosis (34). However, within this mouse model, the source of iron not being associated with amyloid plaques and creating T_2^* differences could be ruled out. Age-matched controls ($n = 4$) did not show T_2^* reduced values and studies on the cerebrovascular angiopathy in this model reported the absence of any hemorrhage (19). This makes APP[V717I] mice a very suitable model for the in vivo study of amyloid plaque formation due to the combination of the amyloid pathology with the oxidative damage common in AD.

In vitro measurements allowed longer acquisition times yielding higher signal-to-noise ratios, which are very useful in T_2^* images for revealing anatomic details. However, brain fixation alters the tissue characteristics compared with living tissue and changes the CNR. We used both in vivo and in vitro MR images acquired with the same parameters for identification of amyloid plaques and concluded that in vivo images, even with their lower power of resolution, suffice for identification of iron-containing plaques in the APP[V717I] mouse model. Histologic stained images and MR images differ in slice thickness and histology is prone to artifacts such as tissue swelling. However, matching of APP anomalies with the underlying cause of iron accumulation is straightforward and pushes along the thalamus as the most affected region.

In conclusion, the reported in vivo and noninvasive detection of amyloid plaques in living APP[V717I] mice using intrinsic MRI contrast resorting from the iron associated with the plaques creates an unexpected opportunity to investigate their longitudinal development in the same animal. Our work is supportive and provides an explanation for the findings on changing T_2^* signal intensity made by Benveniste et al. (11) and the more recent reports from Helpert et al. (13) and Zhang et al. (12). The ability to perform this in vivo in a mouse model allows future correlation studies (1) between the amyloid deposition volume and its deposition site within different mice models, (2) between the disturbed iron metabolism and the amyloid accumulation, and (3) between treated and untreated mice following experimental therapeutic regimes such as amyloid β -structure breaking drugs or vaccinations. Further exploration of A β ligands, which bind amyloid with high affinity, in combination with MR contrast agents (9), together with early detection of T_2^* changes, could contribute to the very early detection of A β plaques.

ACKNOWLEDGMENTS

The authors thank Dr. E. Gilissen for critical reading.

REFERENCES

- Sasaki A, Shoji M, Harigaya Y, Kawarabayashi T, Ikeda M, Naito M, Matsubara E, Abe K, Nakazato Y. Amyloid cored plaques in Tg2576 transgenic mice are characterized by giant plaques, slightly activated microglia, and the lack of paired helical filament-typed, dystrophic neurites. *Virchows Arch* 2002;441:358–367.
- Cai XD, Golde TE, Younkin SG. Release of excess amyloid beta protein from a mutant amyloid beta protein precursor. *Science* 1993;259:514–516.
- Duff K, Eckman C, Zehr C, Yu X, Prada CM, Pereztur J, Hutton M, Buee L, Harigaya Y, Yager D, Morgan D, Gordon MN, Holcomb L, Refolo L, Zenk B, Hardy J, Younkin S. Increased amyloid-beta 42(43) in brains of mice expressing mutant presenilin 1. *Nature* 1996;383:710–713.
- Scheuner D, Eckman C, Jensen M, Song X, Citron M, Suzuki N, Bird TD, Hardy J, Hutton M, Kukull W, Larson E, LevyLahad E, Viitanen M, Peskind E, Poorkaj P, Schellenberg G, Tanzi R, Wasco W, Lannfelt L, Selkoe D, Younkin S. Secreted amyloid beta-protein similar to that in the senile plaques of Alzheimer's disease is increased in vivo by the presenilin 1 and 2 and APP mutations linked to familial Alzheimer's disease. *Nat Med* 1996;2:864–870.
- Suzuki N, Cheung TT, Cai XD, Odaka A, Otvos L Jr, Eckman C, Golde TE, Younkin SG. An increased percentage of long amyloid beta protein secreted by familial amyloid beta protein precursor (beta APP717) mutants. *Science* 1994;264:1336–1340.
- Terwel D, Dewachter I, Van Leuven F. Axonal transport, tau protein, and neurodegeneration in Alzheimer's disease. *Neuromol Med* 2002;2:151–165.
- Vassar R, Bennett BD, Babu-Khan S, Kahn S, Mendiola EA, Denis P, Teplow DB, Ross S, Amarante P, Loeloff R, Luo Y, Fisher S, Fuller L, Edenson S, Lile J, Jarosinski MA, Biere AL, Curran E, Burgess T, Louis JC, Collins F, Treanor J, Rogers G, Citron M. beta-secretase cleavage of Alzheimer's amyloid precursor protein by the transmembrane aspartic protease BACE. *Science* 1999;286:735–741.
- Skovronsky DM, Zhang B, Kung MP, Kung HF, Trojanowski JQ, Lee VMY. In vivo detection of amyloid plaques in a mouse model of Alzheimer's disease. *Proc Natl Acad Sci USA* 2000;97:7609–7614.
- Poduslo JF, Wengenack TM, Curran GL. Targeting of Alzheimer's amyloid plaques. *J Neurochem* 2001;78:129.
- Wadghiri YZ, Sigurdsson EM, Sadowski M, Elliott JI, Li Y, Scholtzova H, Tang CY, Aguinaldo G, Pappolla M, Duff K, Wisniewski T, Turnbull DH. Detection of Alzheimer's amyloid in transgenic mice using magnetic resonance microimaging. *Magn Reson Med* 2003;50:293–302.
- Benveniste H, Einstein G, Kim KR, Hulette C, Johnson A. Detection of neuritic plaques in Alzheimer's disease by magnetic resonance microscopy. *Proc Natl Acad Sci USA* 1999;96:14079–14084.
- Zhang J, Yarowsky P, Gordon MN, Di Carlo G, Munireddy S, van Zijl PCM, Mori S. Detection of amyloid plaques in mouse models of Alzheimer's disease by magnetic resonance imaging. *Magn Reson Med* 2004;51:452–457.
- Helpert JA, Lee SP, Falangola MF, Dyakin VV, Bogart A, Ardekani B, Duff K, Branch C, Wisniewski T, de Leon MJ, Wolf O, O'Shea J, Nixon RA. MRI assessment of neuropathology in a transgenic mouse model of Alzheimer's disease. *Magn Reson Med* 2004;51:794–798.
- Gelman BB. Iron in CNS disease. *J Neuropathol Exp Neurol* 1995;54:477–486.
- Poduslo JF, Wengenack T, Curran GV, Macura S, Borowski B, Jack C, Wisniewski T, Sigurdsson E. Molecular targeting of Alzheimer's amyloid plaques for contrast-enhanced magnetic resonance imaging. *Neurobiol Aging* 2002;23:1550.
- Markesbery WR, Carney JM. Oxidative alterations in Alzheimer's disease. *Brain Pathol* 1999;9:133–146.
- Moechars D, Dewachter I, Lorent K, Reverse D, Baekelandt V, Naidu A, Tesseur I, Spittaels K, Van den Haute C, Checler F, Godaux E, Cordell B, Van Leuven F. Early phenotypic changes in transgenic mice that overexpress different mutants of amyloid precursor protein in brain. *J Biol Chem* 1999;274:6483–6492.
- Dewachter I, Moechars D, van Dorpe J, Tesseur I, Van den Haute C, Spittaels K, Van Leuven F. Modelling Alzheimer's disease in multiple transgenic mice. *Neuron Signal Transduction Alzheimer's Dis* 2001;67:203–210.
- van Dorpe J, Smeijers L, Dewachter I, Nuyens D, Spittaels K, Van den Haute C, Mercken M, Moechars D, Laenen I, Kuiperi C, Bruynseels K, Tesseur I, Loos R, Vanderstichele H, Checler F, Sciot R, Van Leuven F. Prominent cerebral amyloid angiopathy in transgenic mice overexpressing the London mutant of human APP in neurons. *Am J Pathol* 2000;157:1283–1298.
- Kala SV, Hasinoff BB, Richardson JS. Brain samples from Alzheimer's patients have elevated levels of loosely bound iron. *Int J Neurosci* 1996;86:263–269.
- Wengenack TM, Whelan S, Curran GL, Duff KE, Poduslo JF. Quantitative histological analysis of amyloid deposition in Alzheimer's double transgenic mouse brain. *Neuroscience* 2000;101:939–944.
- Bishop GM, Robinson SR, Liu Q, Perry G, Atwood CS, Smith MA. Iron: A pathological mediator of Alzheimer disease?. *Dev Neurosci* 2002;24:184–187.

23. Bodovitz S, Falduto MT, Frail DE, Klein WL. Iron levels modulate alpha-secretase cleavage of amyloid precursor protein. *J Neurochem* 1995;64:307–315.
24. Leveugle B, Spik G, Perl DP, Bouras C, Fillit HM, Hof PR. The iron-binding protein lactotransferrin is present in pathologic lesions in a variety of neurodegenerative disorders: a comparative immunohistochemical analysis. *Brain Res* 1994;650:20–31.
25. Mantyh PW, Ghilardi JR, Rogers S, DeMaster E, Allen CJ, Stimson ER, Maggio JE. Aluminum, iron, and zinc ions promote aggregation of physiological concentrations of beta-amyloid peptide. *J Neurochem* 1993;61:1171–1174.
26. Maynard CJ, Cappai R, Volitakis I, Cherny RA, White AR, Beyreuther K, Masters CL, Bush AI, Li QX. Overexpression of Alzheimer's disease amyloid-beta opposes the age-dependent elevations of brain copper and iron. *J Biol Chem* 2002;277:44670–44676.
27. Qian ZM, Wang Q. Expression of iron transport proteins and excessive iron accumulation in the brain in neurodegenerative disorders. *Brain Res Rev* 1998;27:257–267.
28. Zubenko GS, Farr J, Stiffler JS, Hughes HB, Kaplan BB. Clinically-silent mutation in the putative iron-responsive element in exon 17 of the beta-amyloid precursor protein gene. *J Neuropathol Exp Neurol* 1992; 51:459–463.
29. Bondy SC, Guo-Ross SX, Truong AT. Promotion of transition metal-induced reactive oxygen species formation by beta-amyloid. *Brain Res* 1998;799:91–96.
30. Dhenain M, Duyckaerts C, Michot JL, Volk A, Picq JL, Boller F. Cerebral T2-weighted signal decrease during aging in the mouse lemur primate reflects iron accumulation. *Neurobiol Aging* 1998;19:65–69.
31. Gilissen EP, Jacobs RE, Allman JM. Magnetic resonance microscopy of iron in the basal forebrain cholinergic structures of the aged mouse lemur. *J Neurol Sci* 1999;168:21–27.
32. Aoki S, Okada Y, Nishimura K, Barkovich AJ, Kjos BO, Brasch RC, Norman D. Normal deposition of brain iron in childhood and adolescence: MR imaging at 1.5 T. *Radiology* 1989;172:381–385.
33. Vymazal J, Brooks RA, Zak O, McRill C, Shen C, Di Chiro G. T₁ and T₂ of ferritin at different field strengths: effect on MRI. *Magn Reson Med* 1992;27:368–374.
34. Gelman N, Ewing JR, Gorell JM, Spickler EM, Solomon EG. Interregional variation of longitudinal relaxation rates in human brain at 3.0 T: relation to estimated iron and water contents. *Magn Reson Med* 2001;45:71–79.
35. Dhenain M, Privat N, Duyckaerts C, Jacobs RE. Senile plaques do not induce susceptibility effects in T2*-weighted MR microscopic images. *NMR Biomed* 2002;15:197–203.
36. Pfeifer M, Boncristiano S, Bondolfi L, Stalder A, Deller T, Staufenbiel M, Mathews PM, Jucker M. Cerebral hemorrhage after passive anti-A beta immunotherapy. *Science* 2002;298:1379.
37. Morris CM, Kerwin JM, Edwardson JA. Non-haem iron histochemistry of the normal and Alzheimer's disease hippocampus. *Neurodegeneration* 1994;3:267–275.